Engineering Analysis with Boundary Elements 135 (2022) 26–37

Contents lists available at ScienceDirect

Engineering Analysis with Boundary Elements

journal homepage: www.elsevier.com/locate/enganabound

DEM-BEM coupling in time domain for one-dimensional wave propagation

Guilherme Barros [a,*], Andre Pereira [c], Jerzy Rojek [b], Klaus Thoeni [a]

[a] Centre for Geotechnical Science and Engineering, The University of Newcastle, 2308 Callaghan, Australia
[b] Institute of Fundamental Technological Research, Polish Academy of Sciences, Pawinskiego 5B, 02-106 Warsaw, Poland
[c] Institute of Computing, Fluminense Federal University, Rua Passo da Patria 156, Niterói 24210-240, Brazil

ARTICLE INFO

Keywords:
Discrete Element Method (DEM)
Boundary Element Method (BEM)
Infinite domain coupling
Dynamic multi-scale analysis
Stability of time integration
Spurious wave reflection

ABSTRACT

This work presents a novel scheme to couple the Discrete Element Method (DEM) and the Boundary Element Method (BEM) for the multi-scale modelling in the time domain. The DEM can model discontinuous material at micro scale very well, but it cannot represent infinite domains. Hence, coupling with the BEM is proposed. A formulation employing the DEM and BEM in different subdomains of the same body is presented. There is no overlap between the sub-domains, and the system of equations is derived based on strong equilibrium and compatibility conditions at the interface. The proposed coupling scheme is based on monolithic time integration. The conducted numerical experiments of one-dimensional wave propagation show excellent agreement with the analytical solution. Some spurious wave reflections are observed at the interface, but their effect is quantified and deemed not critical for infinite domains, which are of main interest. Even though the applications for one-dimensional wave propagation are of limited practical engineering interest, this work represents a significant theoretical breakthrough. This paper establishes a reference for future coupling schemes for two- and three-dimensional multi-scale analysis.

1. Introduction

The numerical modelling of wave propagation is of great practical engineering interest. It can be applied to predict the dynamic behaviour of elastic bodies [1], analyse damage detection and determine the elastic properties of the materials [2]. Several continuous and discontinuous based numerical methods are available to solve such problems. While discontinuous methods have the capabilities to represent a model on the micro-scale, continuous methods are more suitable to capture the macroscopic behaviour. Among the methods that treat the domain as a continuous media, it is worth mentioning the Finite Difference Method (FDM), the Finite Element Method (FEM), and the BEM, whereas the main method that models the domain discontinuously is the DEM [3].

The coupling between the DEM and a continuous method allows for multi-scale modelling, employing various material models at different scales in different parts of the same domain. This coupling also improves the computational efficiency of the DEM, which is critical to real-life problems [4–6]. DEM is a suitable tool for modelling geometric and physical non-linearities [7–11]. The FEM is the most common continuous method used for multi-scale modelling. One of the first attempts in that direction seems to be the work of Oñate and Rojek [12], who defined a contact model between the Discrete Element (DE) particle and the Finite Element (FE) edge. Since then, much work has been developed on the coupling of DEM and FEM. It is worth mentioning the work by Azevedo and Lemos [13], who coupled the two methods using an interface coupling approach. However, Rojek and Oñate [14] realised that the interface approach produces spurious wave reflection at the interface and, consequently, proposed a coupling method, extending the work of Xiao and Belytschko [15], with an overlapping region also called bridging domain.

A large number of DEM-FEM coupling techniques are presented in the scientific literature. Rousseau et al. [5] used a bridging domain approach to study impact analysis on concrete structures. Elmekati and Shamy [16] presented a staggered interface coupling using different time steps to model geotechnical systems, such as piles installed in granular soil. Li and Wan [17] used the bridging scale method to couple the DEM with a Cosserat continuum modelled by the FEM. Wellmann and Wriggers [18] coupled the DEM with the FEM using an elasto-plastic constitutive model whose parameters are determined from the particles via homogenisation. Dang and Meguid [19] used coupled DEM-FEM to model quasi-static nonlinear soil–structure interaction problems. Xu and Zang [20] proposed a methodology to couple the rotations of DE particles with the FEM and applied it to modelling the brittle fracture of laminated glass. Tu et al. [21] proposed a generalised bridging domain method and showed that several overlapping coupling

* Corresponding author.
E-mail address: Guilherme.CoelhoGomesBarros@uon.edu.au (G. Barros).

https://doi.org/10.1016/j.enganabound.2021.10.017
Received 18 August 2021; Received in revised form 24 October 2021; Accepted 26 October 2021

Table 1
Coupling methods for DEM and continuous methods.
Source: Modified after Tu et al. [22].

Method	Derivation of governing equations	Width of the coupling domain	Compatibility condition	Avoiding spurious reflections
Bridging scale decomposition method [17,25]	Energy-based	Finite	Weak and strong mixed, mutually prescribed	Yes
Bridging domain method [5,14,15,18,26,27]	Energy-based	Finite	Weak, mutually prescribed	Yes
Edge-to-edge coupling method [13,16,19,20]	Energy-based or force-based	Zero	Weak or strong, mutually prescribed	No
Separate domain coupling method [21]	Force-based	Finite	Weak, separately prescribed	Yes
Separate edge coupling method [21,22]	Force-based	Finite	Weak, separately prescribed	Yes

techniques are particular cases of that general formulation. Later, Tu et al. [22] investigated further the separate edge method to couple DEM and FEM. More recently, Tu et al. [23] studied stress continuity in DEM-FEM multi-scale coupling.

The main differences among coupling approaches can be distinguished based on three aspects: (i) formulation, (ii) coupling domain, and (iii) compatibility condition. There are two possible formulations, the energy-based, derived from the minimisation of an energy functional, and the force-based, where equilibrium equations are explicitly satisfied [24]. The coupling takes place either at the interfacing boundary or over a finite overlapping domain. The compatibility condition can be enforced in either a strong or a weak sense. In addition, this condition can be imposed separately, as in the iterative coupling, or simultaneously, as in the direct coupling. Table 1 lists a summary of existing literature on coupling DEM with continuous methods.

Although the DEM-FEM coupling is a well-developed multi-scale modelling technique, its application to practical dynamic problems is limited because many real-life applications involve infinite domains, which are difficult to model with DEM and FEM. Among real-life problems involving an infinite or semi-infinite domain, one could list the radiation of heat from a point source into space and the propagation of waves in the ground due to an earthquake or blasting. In such problems, the strength of the heat radiation and the amplitude of the waves vanish at infinity. In static and quasi-static analyses, one can truncate the infinite domain and study the area of interest. That is possible using DEM, FEM and both coupled. However, in dynamic simulations, truncation results in wave reflections that alter the response of the area of interest.

The BEM is an established numerical method that performs exceptionally well in infinite domains problems [28] since its formulation uses fundamental solutions that allow for domain integrals to be eliminated [29]. It reduces the order of discretisation by one compared to other continuous numerical methods, hence, it is very efficient. BEM application to dynamic analyses is a more recent yet promising field, being successfully applied to dynamic simulations of infinite domains [30,31]. Therefore, coupling the DEM with the BEM allows for multi-scale coupling with improved modelling capabilities. However, only a few attempts have been made to couple the two methods, mainly due to the complexity of the BEM formulation. To the authors' best knowledge, the few existing approaches for coupling the DEM with BEM consider a quasi-static formulation for the BEM [32,33]. These approaches are not able to correctly predict the dynamic response of the BEM domain. Moreover, the only paper available in the literature for time-domain DEM-BEM coupled analysis relies on a FEM interface layer [34].

The main contribution of the current paper is to overcome this limitation by presenting a coupled multi-scale DEM-BEM formulation entirely in the time domain. Herein a formulation is proposed to successfully couple the aforesaid methods. This formulation does not rely on any other method. The multi-scale coupling uses the DEM and the BEM to model the microscopic and the macroscopic behaviours, respectively. This coupling technique excels by employing groundbreaking BEM formulations in the time domain [35,36]. An interface approach is employed, and a force-based formulation is used, *i.e.* the system of equations is derived by direct imposition of the equilibrium equation at the interface. Moreover, the coupling takes place at the interfacing boundary only so that no overlap region is required. Furthermore, the compatibility conditions are imposed strongly and mutually in both methods.

In order to present the formulations and findings of this paper, firstly, the differential equation for one-dimensional wave propagation is introduced (Section 2). The solution of such equation by DEM and BEM, independently, is shown in Section 3. After enunciating the main equations of each numerical method, Section 4 presents how to modify them so that it is possible to perform the coupling. With the complete framework, some benchmark problems are solved to analyse the accuracy and nuances of the coupled DEM-BEM solution. These results are reported in Section 5. Lastly, the discussions about the results and conclusions of what was presented are available in Section 6.

2. One-dimensional wave propagation

The study of wave propagation in one-dimensional media (Fig. 1(a)) comprehends the understanding of how waves propagate within an elastic body. Elastic waves are caused by dynamic effects, such as dynamic loading, and are governed by the following differential equation [1]

$$\frac{\partial^2 u}{\partial x^2} = \frac{1}{c^2}\frac{\partial^2 u}{\partial t^2}\,, \tag{1}$$

where u, the axial displacement, is a function of space x and time t and c is the scalar wave velocity of the material defined as

$$c = \sqrt{\frac{E}{\rho}}\,. \tag{2}$$

where E and ρ are the Young's modulus and mass density of the material, respectively. Therefore, Eq. (1) can be rewritten as

$$\rho\frac{\partial^2 u}{\partial t^2} - E\frac{\partial^2 u}{\partial x^2} = 0\,, \tag{3}$$

in which the first term relates to the kinetic energy, while the second relates to strain energy. The axial internal force N, resulting from axial stresses acting over the cross section area A, is given by

$$N = EA\frac{\partial u}{\partial x}\,. \tag{4}$$

The solution of the wave propagation problem needs to satisfy not only the differential equation in Eq. (1) but also the boundary conditions. The boundary conditions can be either an applied displacement or an applied force. For instance, the cantilever example shown in Fig. 1(b) has the following boundary conditions: $N(0,t) = -P(t)$

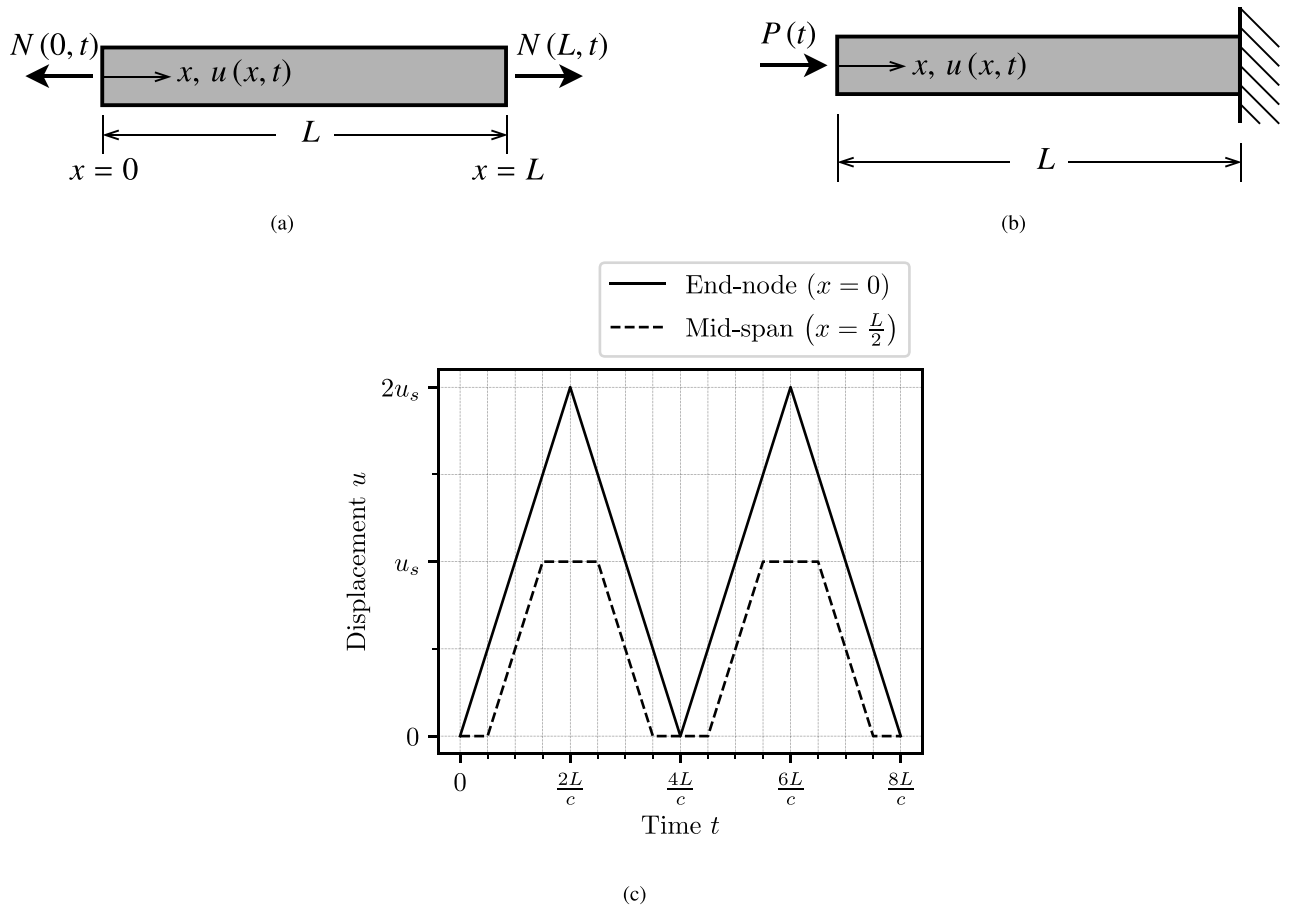

Fig. 1. Wave propagation in an one-dimensional rod under compression: (a) general problem of wave propagation in one-dimension, (b) cantilever problem and (c) its analytical solution.

and $u(L,t) = 0$. The corresponding analytical response is depicted in Fig. 1(c), where

$$u_s = \frac{PL}{EA} \tag{5}$$

is the static solution of the displacement of the free-end node. The analytical solution presented in Fig. 1(c) is used for validating the numerical models presented in the following sections.

3. Numerical framework

In this section, the classical formulation of both the DEM and BEM are described. In both methods, and in the coupled solution presented hereafter, a constant time step Δt is used throughout the analysis. The total time of analysis ranges from 0 to T, *i.e.* $t \in [0, T]$. Employing the time stepping procedure, one may write $T = N\Delta t$ and $t = n\Delta t$ with $n = 0, \ldots, N$. In addition, it shall be pointed out that the displacement field $u(x,t)$ is replaced by nodal displacements, in the DE particles or BEM nodes. They are grouped in the displacement vector $\boldsymbol{d}(t)$, whose derivative with respect to time furnishes the nodal velocity vector $\boldsymbol{v}(t) = \frac{\mathrm{d}\boldsymbol{d}(t)}{\mathrm{d}t}$. Consecutively, the nodal acceleration vector is given by $\boldsymbol{a}(t) = \frac{\mathrm{d}\boldsymbol{v}(t)}{\mathrm{d}t} = \frac{\mathrm{d}^2\boldsymbol{d}(t)}{\mathrm{d}t^2}$.

3.1. Discrete Element formulation

The DEM is a suitable method for modelling the microscopic behaviour since its formulation consists on discretising the domain in particles that interact through contact laws on the micro-scale. Particles can be any closed subset of the domain. Commonly, spheres and discs are used for three and two-dimensional analyses, respectively, as they simplify contact detection. In one-dimension, the domain can only take the form of an interval, so DE particles are consequently intervals or segments. Furthermore, the segments can be represented as mass points, which in the following are referred to as particles. In the classical DE formulation, particles and interactions are taken into account at each time step to form the differential equation of motion

$$\boldsymbol{M}\boldsymbol{a}(t) = \boldsymbol{f}_{\mathrm{R}}(t)\,, \tag{6}$$

where $\boldsymbol{M}$ is the diagonal mass matrix, $\boldsymbol{a}$ is the acceleration vector and $\boldsymbol{f}_{\mathrm{R}}$ is the resultant force vector, all at time t. Furthermore, the resultant force vector is composed of applied forces $\boldsymbol{f}$ and contact forces $\boldsymbol{f}_{\mathrm{C}}$, *i.e.* $\boldsymbol{f}_{\mathrm{R}} = \boldsymbol{f}_{\mathrm{C}} + \boldsymbol{f}$. The contact forces $\boldsymbol{f}_{\mathrm{C}}$, here only acting in normal direction, follow a cohesive model and can be calculated as a function of the displacement vector $\boldsymbol{d}$ as

$$\boldsymbol{f}_{\mathrm{C}} = -\boldsymbol{K}\boldsymbol{d}(t)\,, \tag{7}$$

where $\boldsymbol{K}$ is the stiffness matrix based on a linear normal contact law. Thereby, Eq. (6) can be written as

$$\boldsymbol{M}\boldsymbol{a}(t) + \boldsymbol{K}\boldsymbol{d}(t) = \boldsymbol{f}(t)\,. \tag{8}$$

In order to simulate a problem governed by Eq. (1) using DEM, the mass of each particle and the stiffness of each interaction must reflect its macroscopic parameters. The first terms in Eqs. (3) and (6) are related to kinetic energy, while the second terms are related to deformation energy. Therefore, to best simulate a problem governed by Eq. (1) the mass of each particle p should be taken as

$$m_p = \rho A \ell_p\,, \tag{9}$$

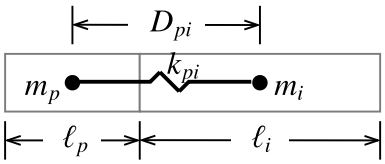

Fig. 2. DE particles (*i.e.* segments) and interactions among them.

where ℓ_p is the length of the particle. Furthermore, the stiffness of an interaction between particles p and i is given by

$$k_{pi} = \frac{EA}{D_{pi}}, \tag{10}$$

where D_{pi} is the distance between the centre of the two particles, as schematically shown in Fig. 2.

Another topic of discussion is how to properly discretise the domain into particles. Fig. 3 shows three different possible discretisations:

- Model A (Fig. 3(a)): Particles are actual subsets of the rod's domain, *i.e.* particles are enclosed in the rod's domain. Therefore, the total mass of the model is exactly equal to the rod's mass, however, the effective length for wave propagation is smaller than the rod's length.
- Model B (Fig. 3(b)): Particles are centred on the rod's endpoints as well as in its interior. In that way, the effective length is exactly equal to the rod's length but the total mass is higher since half of the particles on the endpoints are located outside the rod's domain.
- Model C (Fig. 3(c)): The same as Model B but the mass of the endpoint particles are reduced by half in order to achieve consistency with the mass of the rod.

Model A seems the most logical choice since particles are indeed a subset of the domain. However, since the mass of the particles are lumped in their centre and all forces are applied in those points, the effective length $\tilde{L}$ within which the wave propagates is smaller than the rod's actual length L. Model B eliminates this issue as the centres of the first and last particle correspond to the end nodes of the rod. However, particles whose centre correspond to the end-nodes of the rod contain mass that is not in the original domain. Moreover, the total mass of the discrete model $\tilde{M}$ exceeds the mass of the original model M. In order to correct this, the mass of those particles can be taken as half of the one in Eq. (9), which corresponds to Model C.

Intuitively, all three models should converge to the same response as the discretisation gets finer. In Model A, the effective length approaches to the original one as the particles get smaller. In Model B and C, the mass outside the original domain tends to zero as particles become smaller. Section 5.1.1 will discuss this in more detail.

After completely defining the spatial discretisation, another key aspect of the DEM is the time integration scheme applied to it. The most used explicit time integration method is a variant of the Central Difference (CD) method. This method is called the Verlet time integration scheme or the "leapfrog" method. In this method, the acceleration vector $\boldsymbol{a}$ is calculated from the known forces (external and contact forces) at time t. From that, the velocity vector $\boldsymbol{v}$ is determined for an intermediate step $t + \Delta t/2$. Finally, the displacement vector $\boldsymbol{d}$ is computed at time $t + \Delta t$, in other words,

$$\begin{aligned} \boldsymbol{v}\left(t + \frac{\Delta t}{2}\right) &= \boldsymbol{v}\left(t - \frac{\Delta t}{2}\right) + \Delta t \boldsymbol{a}(t), \\ \boldsymbol{d}(t + \Delta t) &= \boldsymbol{d}(t) + \Delta t \boldsymbol{v}\left(t + \frac{\Delta t}{2}\right). \end{aligned} \tag{11}$$

Since this is an explicit time integration scheme, the time step chosen plays a fundamental role. Namely, the time step cannot exceed a so-called critical value. Beyond this value, the integration scheme will no longer be numerically stable. The work of Otsubo et al. [37] presents a compilation of theoretical values of critical time steps as well as numerical experiments. The critical time step can be found solving the generalised eigenvalue problem

$$\left(\boldsymbol{K} - \omega^2 \boldsymbol{M}\right) \boldsymbol{\phi} = \boldsymbol{0}, \tag{12}$$

where, ω is a natural frequency of the system (square root of the eigenvalue), associated with the vibration mode (eigenvector) $\boldsymbol{\phi}$. The critical time step is then calculated from the maximum natural frequency $\omega_{\max}$ as

$$\Delta t_{\text{crit}} = \frac{2}{\omega_{\max}}. \tag{13}$$

Fig. 4 shows the critical time step Δt_{crit}, calculated using Eq. (13), for each DE model varying the number of particles. It can be seen that the critical time step decreases with the increase of the number of particles for all three models. The critical time step for Model B is always bigger than the one for Models A and C. For less than 15 particles, Model A and C have a similar critical time step. For a discretisation with more than 15 particles, the time step of Model A converges to the one of Model B and Model C becomes the one with the smallest critical time step.

3.2. Boundary Element formulation

The BEM employs macroscopic models based on the continuum theory. The formulation used in this paper follows the one presented by Moser et al. [35], which is based on the Duhamel integral. The Duhamel integral allows the dynamic response of a linear system to be evaluated as a convolution integral [38,39]. The concept was employed to formulate dynamic equilibrium equations in terms of displacements. Therefore, the force vector at time t, $\boldsymbol{f}(t)$, may be calculated as

$$\boldsymbol{f}(t) = \int_0^t \boldsymbol{K}(t - \tau)\, \boldsymbol{d}(\tau)\, \mathrm{d}\tau, \tag{14}$$

which is the convolution integral between the forces per displacement and time $\boldsymbol{K}(t - \tau)$ at time t, resulting from the application of a unit impulse displacement at time τ, with the applied displacements $\boldsymbol{d}(\tau)$ at time τ. Some elastodynamic formulations of the BEM try to solve this equation by applying a time interpolation [30,40]. However, these techniques are very numerically unstable [31].

To work around this issue, the Convolution Quadrature Method (CQM) can be used [31,41,42]. The CQM allows the integral in Eq. (14) to be computed as a weighted summation. By doing so, Eq. (14) becomes

$$\boldsymbol{f}(n\Delta t) \approx \sum_{k=0}^{n} \boldsymbol{w}_{n-k}\left(\hat{\boldsymbol{K}}, \Delta t\right) \boldsymbol{d}(k\Delta t). \tag{15}$$

The weights $\boldsymbol{w}_{n-k}\left(\hat{\boldsymbol{K}}, \Delta t\right)$ are calculated based on the solution of the unit impulse in the Laplace domain $\hat{\boldsymbol{K}}$, the time step Δt adopted in the numerical solution, the number of steps n taken until t, since $t = n\Delta t$, and the number of steps k in the convolution integral, since $\tau = k\Delta t$. Hence, $t - \tau = (n - k)\Delta t$. Thereby, the solution for the unit impulse in the time domain is not necessary and the solution in the Laplace domain is relatively easy to determine [35].

Schanz [31] noted that the adopted time step plays a critical role in the stability of the numerical solution. On the one hand, the time history might not be properly captured with large time steps and significant numerical damping may appear. On the other hand, if the time step is chosen too small, numerical instabilities arise.

As only the boundary (*i.e.* end-nodes for the one-dimensional case) is considered in the BEM, the calculation of results at internal points becomes a post-processing task. It can be carried using the Duhamel integral, as

$$\boldsymbol{d}_{\text{int}}(t) = \int_0^t \boldsymbol{H}(t - \tau)\, \boldsymbol{d}(\tau)\, \mathrm{d}\tau, \tag{16}$$

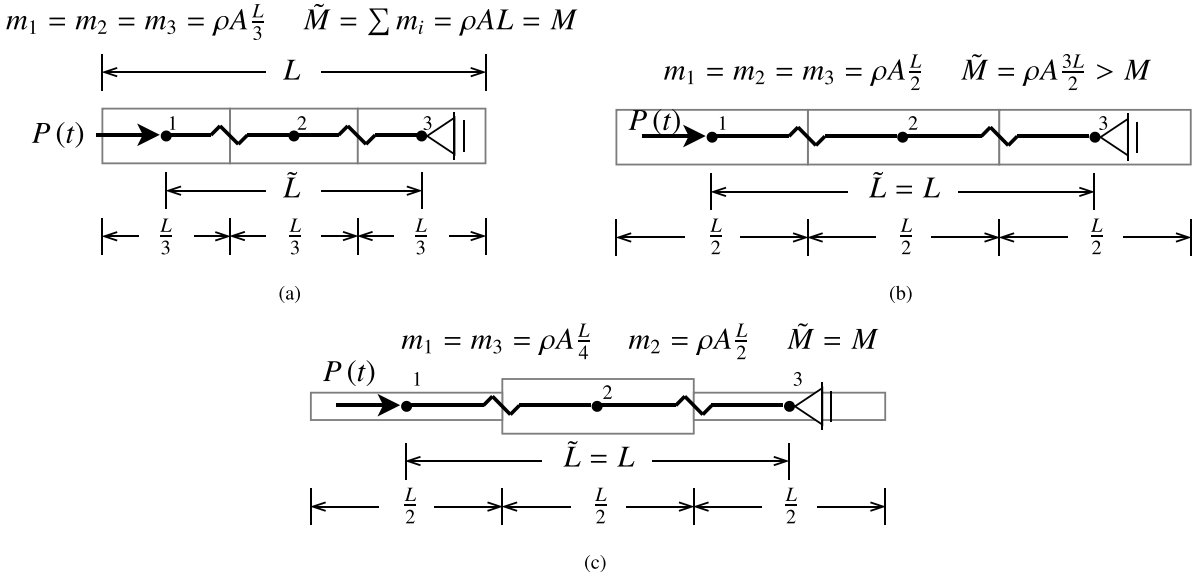

Fig. 3. Different discretisation approaches for a three-particle example: (a) Model A: particles are enclosed in the rod's domain ($\tilde{L} < L$ and $\tilde{M} = M$), (b) Model B: particles are centred on the rod's endpoints as well as in its interior ($\tilde{L} = L$ and $\tilde{M} > M$), and (c) Model C: particles at both ends have corrected masses ($\tilde{L} = L$ and $\tilde{M} = M$).

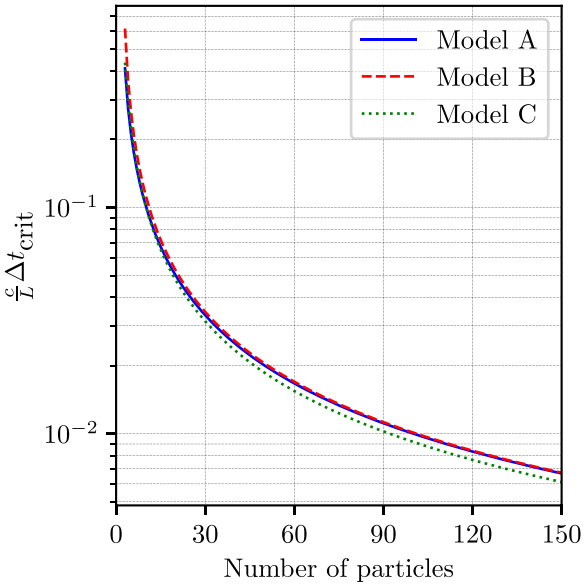

Fig. 4. Critical time step varying the number of particles, using different modelling approaches. (For interpretation of the references to colour in this figure legend, the reader is referred to the web version of this article.)

where, $\boldsymbol{H}(t-\tau)$ is the response of the system at a internal point caused by unit impulse displacements of the boundary's nodes. The evaluation of Eq. (16) can also be carried out through the CQM, thus

$$\boldsymbol{d}_{\text{int}}(n\Delta t) \approx \sum_{k=0}^{n} \boldsymbol{w}_{n-k}\left(\hat{\boldsymbol{H}}, \Delta t\right) \boldsymbol{d}(k\Delta t)\,, \tag{17}$$

where the internal point displacement caused by the boundary node displacements is calculated in the Laplace domain $\hat{\boldsymbol{H}}$.

4. Coupling

In this work, the BEM and DEM are coupled to simultaneously model Eq. (1) on different scales. The challenge in making such coupling feasible relies on two different fundamentals. From the modelling point of view, the DEM describes the domain as a discontinuous media while the BEM follows a continuous approach. From the mathematical point of view, the DEM integrates the differential equation of motion, whereas the BEM performs a convolution integral. Due to these differences, the coupling between the two methods in the time domain is quite complex and modifications are necessary in both methods to make this possible.

The modifications proposed consist of writing the equations of both methods for each time step as a stiffness like equation, *i.e.* for the BEM

$$\tilde{\boldsymbol{K}}_{\text{B}}\boldsymbol{d}_{\text{B}}^{(n)} = \boldsymbol{p}_{\text{B}}^{(n)} + \tilde{\boldsymbol{p}}_{\text{B}}^{(n)}\,, \tag{18}$$

and for the DEM

$$\tilde{\boldsymbol{K}}_{\text{D}}\boldsymbol{d}_{\text{D}}^{(n)} = \boldsymbol{p}_{\text{D}}^{(n)} + \tilde{\boldsymbol{p}}_{\text{D}}^{(n)}\,, \tag{19}$$

where $\tilde{\boldsymbol{K}}$ is a dynamic stiffness matrix, $\boldsymbol{d}^{(n)}$ and $\boldsymbol{p}^{(n)}$ are the displacement and the force vectors at time step n, respectively, and $\tilde{\boldsymbol{p}}^{(n)}$ is the force vector accounting for the effects of the previous time steps. In addition, the subscripts B and D stand for BEM and DEM, respectively. Writing the equation in such way for both methods allows a straightforward coupling via stiffness matrices. Hence a global system of equations can be assembled as

$$\tilde{\boldsymbol{K}}\boldsymbol{d}^{(n)} = \boldsymbol{p}^{(n)} + \tilde{\boldsymbol{p}}^{(n)}\,. \tag{20}$$

As mentioned in Section 3.1, time integration for the DEM is generally carried out using the explicit "leapfrog" or Verlet scheme. In the current formulation, this scheme is substituted by the CD algorithm [43]. Using the CD algorithm, it is also possible to write an equation like Eq. (19) with a dynamic stiffness relation between displacements and forces at instant $t = n\Delta t$.

The CD method is based on the finite difference approximation of the time derivatives of displacements. Therefore, the central differences for velocity and acceleration are given by

$$\boldsymbol{v}^{(n)} = \frac{\boldsymbol{d}_{\text{D}}^{(n+1)} - \boldsymbol{d}_{\text{D}}^{(n-1)}}{2\Delta t}\,, \tag{21}$$

and

$$\boldsymbol{a}^{(n)} = \frac{\boldsymbol{d}_{\text{D}}^{(n+1)} - 2\boldsymbol{d}_{\text{D}}^{(n)} + \boldsymbol{d}_{\text{D}}^{(n-1)}}{\Delta t^2}\,, \tag{22}$$

respectively. Substituting Eq. (22) in Eq. (6) leads to

$$\tilde{\boldsymbol{K}}_{\text{D}} = \frac{\boldsymbol{M}}{\Delta t^2}\,,\ \boldsymbol{p}_{\text{D}}^{(n)} = \boldsymbol{0}\,, \tag{23}$$

(a) (b)

Fig. 5. Different approaches for modelling the DEM-BEM interface: (a) coupling the displacement of the DE particle centre with BE end-node displacement (lighter grey indicates overlap, reason why the particle must have half the mass) and (b) coupling through an interaction model between the DE particle and the BE region.

and

$$\tilde{\boldsymbol{p}}_{\mathrm{D}}^{(n)} = \boldsymbol{p}_{\mathrm{D}}^{(n-1)} + \left(\frac{2\boldsymbol{M}}{\Delta t^2} - \boldsymbol{K}\right)\boldsymbol{d}_{\mathrm{D}}^{(n-1)} - \frac{\boldsymbol{M}}{\Delta t^2}\boldsymbol{d}_{\mathrm{D}}^{(n-2)} . \tag{24}$$

For the BEM, a simple reordering is needed in order to cast Eq. (15) into Eq. (18). It is possible to write

$$\tilde{\boldsymbol{K}}_{\mathrm{B}} = \boldsymbol{w}_0\left(\hat{\boldsymbol{K}}, \Delta t\right) , \tag{25}$$

and

$$\tilde{\boldsymbol{p}}^{(n)} = \sum_{k=0}^{n-1} \boldsymbol{w}_{n-k}\left(\hat{\boldsymbol{K}}, \Delta t\right)\boldsymbol{d}\left(k\Delta t\right) . \tag{26}$$

From the DE modelling discussions (Fig. 3), two possibilities arise to model the interface between DEM and BEM. The first is to place a particle with half the mass at the interface, *i.e.* at the end-node of the Boundary Element (BE) region (Fig. 5(a)). The half-mass approach is used to account for the fact that half of the DE particle overlaps with the BE region. The second possibility is to make the intersection between the particle and the BE region a single point – the BE region end-point – and add a DE interaction between the particle and the BE region end-node (Fig. 5(b)).

The modelling alternative shown in Fig. 5(a) couples DEM with BEM in an interface approach. Therefore, the contribution to the dynamic stiffness matrix of the BE and the DE particle at the interface is summed up. Hence, if an assembly of P particles is coupled in that fashion with a finite BE region, the global matrix of the system will be

$$\tilde{\boldsymbol{K}} = \begin{bmatrix} \frac{m_1}{\Delta t^2} & 0 & \dots & 0 & 0 \\ 0 & \frac{m_2}{\Delta t^2} & \dots & 0 & 0 \\ \vdots & \vdots & \ddots & \vdots & \vdots \\ 0 & 0 & \dots & \frac{m_P}{\Delta t^2} + \left(\tilde{k}_{\mathrm{B}}\right)_{1,1} & \left(\tilde{k}_{\mathrm{B}}\right)_{1,2} \\ 0 & 0 & \dots & \left(\tilde{k}_{\mathrm{B}}\right)_{2,1} & \left(\tilde{k}_{\mathrm{B}}\right)_{2,2} \end{bmatrix} . \tag{27}$$

The modelling option shown in Fig. 5(b) defines a contact coupling. In this kind of coupling, a specific interaction (*i.e.* contact model) needs to be defined between the DE particle and the BE region. Hence, the dynamic stiffness matrix does not have terms correlating these elements, and the only effect of the particle on the BE domain appears in the computation of the force vector. It is worth pointing out that the interface modelling option presented in Fig. 5(b) furnishes a global system of equations with one more degree of freedom than the one obtained using Fig. 5(a). Therefore, the global matrix found from contact coupling between a P-particle assembly and a finite BE region is

$$\tilde{\boldsymbol{K}} = \begin{bmatrix} \frac{m_1}{\Delta t^2} & \dots & 0 & 0 & 0 \\ \vdots & \ddots & \vdots & \vdots & \vdots \\ 0 & \dots & \frac{m_P}{\Delta t^2} & 0 & 0 \\ 0 & \dots & 0 & \left(\tilde{k}_{\mathrm{B}}\right)_{1,1} & \left(\tilde{k}_{\mathrm{B}}\right)_{1,2} \\ 0 & \dots & 0 & \left(\tilde{k}_{\mathrm{B}}\right)_{2,1} & \left(\tilde{k}_{\mathrm{B}}\right)_{2,2} \end{bmatrix} . \tag{28}$$

5. Results

5.1. Finite homogeneous rod

A finite rod with a length $L = 10\,\mathrm{m}$ and a cross-section area $A = 1\,\mathrm{cm}^2$ made of homogeneous material with Young's modulus $E = 210\,\mathrm{GPa}$ and mass density $\rho = 7850\ \mathrm{kg/m}^3$ is considered. The rod is fixed on the right-hand side and subjected to a Heaviside load of magnitude $P_0 = 21\,\mathrm{kN}$ on the left-hand side (Fig. 1(b)). The rod is used as a benchmark problem for carrying out a convergence study on the discretisation on both time and space.

The analytical solution shown in Fig. 1(c) is dependent on both time and space. Therefore, a dimensionless scalar error measurement is introduced to investigate the performance of both numerical methods. The overall relative error ϵ is defined as

$$\epsilon = \frac{\int_0^L \int_0^T |d - u| \,\mathrm{d}t\mathrm{d}x}{\int_0^L \int_0^T u \,\mathrm{d}t\mathrm{d}x} , \tag{29}$$

where d and u are the numerical and analytical solutions respectively, and T is the total time of analysis assumed to be 25 ms. Eq. (29) takes into account errors throughout the rod's domain and observation time in an integral form. Hence, it is a better error indicator than evaluating the difference on a single point at a specific instant.

5.1.1. Pure DEM analysis

The three different discrete element discretisations shown in Fig. 3 are used to model the rod problem. First, the convergence of space discretisation is analysed and the time step is kept fixed. The convergence curves for the three models are depicted in Fig. 6. For all analyses, *i.e.* for all discretisation models and refinement, the time step is kept fixed at $\Delta t = 1 \times 10^{-5}$ s. This time step is lower than the critical time step, as can be seen from Fig. 4. The results of Model A are plotted as a solid blue line, whereas the results for Model B and Model C are plotted as a dashed red line and a dotted green line, respectively. It can be seen that Model C converges faster than Model A and B, as it preserves the effective length and overall mass of the original problem.

The error map of the numerical solution using pure DEM with Model C, 151 particles and $\Delta t = 1 \times 10^{-5}$ s is shown in Fig. 7. In this case, the overall relative error, as defined in Eq. (29), is $\epsilon = 1.29 \times 10^{-3}$. The error map shows the absolute difference between the analytical solution and the numerical prediction for each position x and time t using a colour map. It can be seen that the difference is higher where the derivative of the analytical solution of the displacements with respect to time is discontinuous, *i.e.* where the velocity jumps. Moreover, it is clear from Fig. 7 that this difference increases as the analysis time increases.

5.1.2. Pure BEM analysis

Analysing the problem of Fig. 1 using the BEM requires no domain discretisation. Therefore, only a convergence study on the time step is required. The error, as described in Eq. (29), demands a domain integration, which is carried out using the trapezoidal integration rule after the computation of forces and displacements at internal points. The overall relative error for simulations with different time steps is plotted in Fig. 8(a) and Fig. 8(b) for a single BE region and two BE regions, respectively. It can be inferred that the smaller the time step the smaller the error.

However, from Fig. 8(a), it can be understood that for a single BE region the time step cannot be lowered beyond 1.12×10^{-2} ms. If a smaller time step is chosen, the programme simply crashes due to the presence of numbers greater than the floating-point capacity in the computation of the CQM weights. On the other hand, large time steps lead to a lack of stability. It can be seen in Fig. 8 that the response becomes unstable for $\Delta t > 1$ ms.

The time step of the analysis can be lowered using a multi-region technique, *i.e.* by splitting the rod in several BE sub-regions. Therefore,

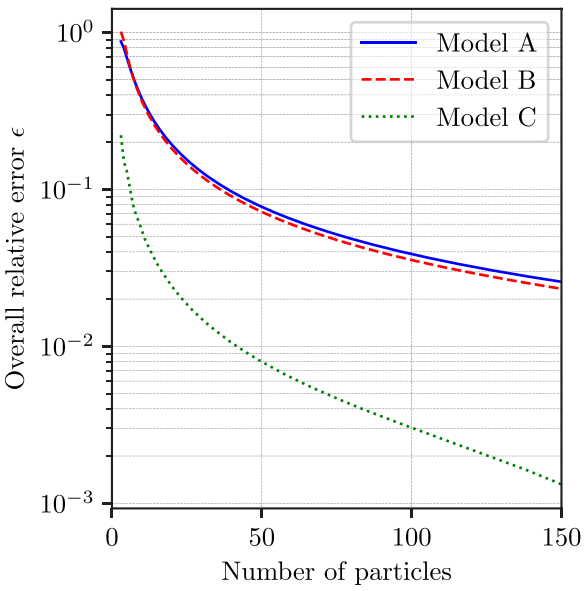

Fig. 6. Discretisation convergence study for different DE models using $\Delta t = 1 \times 10^{-5}$ s. (For interpretation of the references to colour in this figure legend, the reader is referred to the web version of this article.)

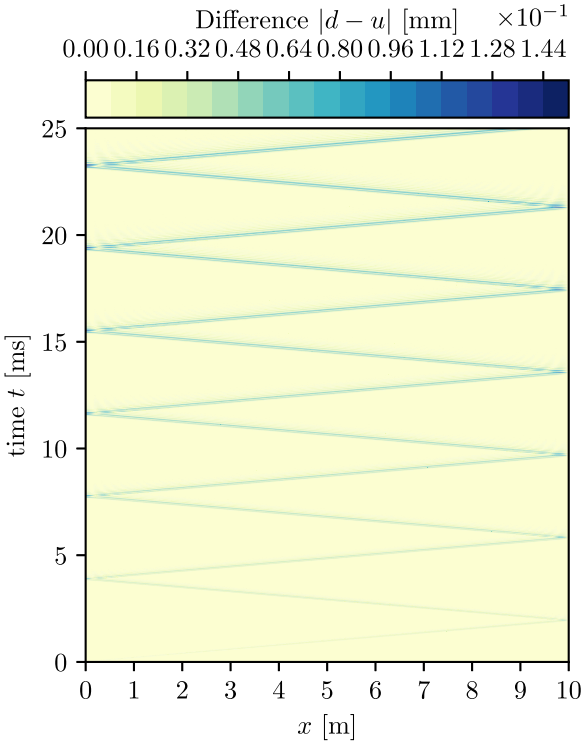

Fig. 7. Error map of pure DEM results using Model C with 151 particles and $\Delta t = 1 \times 10^{-5}$ s.

the same time step convergence study is carried out using two symmetrical BE regions. The plot of the overall error versus time step is shown in Fig. 8(b). It can be observed that the error is the same for one and two BE regions when the same time step is used. However, an advantage in using two BE regions can be noticed: the minimum time step required for numerical stability can be lowered from 1.12×10^{-2} ms to 5.62×10^{-3} ms which results in a lower overall relative error.

The error map of the pure BEM analysis using two BE regions is shown in Fig. 9. The results were obtained using a time step of 1×10^{-5} s, which is within the range of stability. This time step is chosen to make the pure BEM and pure DEM results comparable. The overall error found for this model is 6.08×10^{-3}, which is in the same order of magnitude as the error observed in the pure DEM analysis. As in pure DEM, the most substantial errors occur in the vicinity of the analytical response's discontinuities and the errors increase as the analysis progresses in time.

5.1.3. Coupled DEM-BEM analysis

The proposed coupled DEM-BEM algorithm is employed in the finite homogeneous rod problem (Fig. 1(b)). Both approaches are shown in Fig. 5 for modelling the interface between the two domains are tested. The main aim of this analysis is to compare the performance of each approach for different numbers of particles in the DEM domain. The end-node of the DEM domain is modelled using the effective end-node with the half-mass correction (Fig. 3(c)).

The results obtained by modelling the loaded half of the domain with DEM and the supported half with BEM are plotted in Fig. 10(a). The number of particles in Model A (Fig. 5(a)) is increased by one so that the number of degrees of freedom in both models is the same. In order to perform further investigations, the methods are swapped – *i.e.* the loaded half is modelled with BEM and the supported with DEM – and the convergence in this configuration is depicted on Fig. 10(b). It can be seen that in both cases the error has the same order of magnitude. Note that all analyses have been performed with a time step $\Delta t = 1 \times 10^{-5}$ s, which is lower than the critical time step of the DEM (Fig. 4) and is within the range of numerical stability for the BEM (Fig. 8).

It can be seen that the relative error is almost identical for both interface models. Both solutions converge to a relative error of about 2.01×10^{-2}. The two convergence curves have similar shapes, either using BEM or DEM on the loaded half of the domain. It is interesting to note that the error is one order of magnitude bigger than the ones obtained with pure BEM and pure DEM, using an equivalent number of particles.

The error map for the coupled DEM-BEM analysis using DEM on the loaded part of the domain is shown in Fig. 11(a), while the one using BEM on the loaded part of the domain is shown in Fig. 11(b). In both cases, Model A was used at the interface. 76 particles were used and the time step was set to 1×10^{-5} s. In both error maps in Fig. 11, it is possible to observe that the error distribution is significantly different between the pure DEM and pure BEM results. The errors in the coupled DEM-BEM analyses are much higher where the analytical solution is continuous and these errors increase over time.

Apart from the approximation errors introduced by each method, another critical source of error is the spurious wave reflection at the interface. The presence of this phenomenon is evidenced in Fig. 12. The time response obtained with the coupled DEM-BEM approach using Model A (Fig. 5(a)) is shown alongside the difference from the response obtained with pure DEM. 151 particles were used in the pure DEM analysis, while 76 particles were used in the coupled DEM-BEM analysis. In both analyses the time step used was the same ($\Delta t = 1 \times 10^{-5}$ s).

The response is plotted from the initial configuration to half of the first period of oscillation, $\frac{2L}{c}$. This time range is enough to observe the spurious wave reflection. The displacement of the end-node is plotted as a solid blue line, while the mid-span displacement is plotted as a dash-dotted red line. The difference between DEM-BEM and pure DEM is plotted as a dashed black line for the end-node and dotted green line for the mid-span.

From Fig. 12 it can be inferred that the error on both nodes is zero until the mid-span node starts to move, *i.e.* when the dash-dotted line starts to increase. That point is exactly at the interface between the two domains. The difference of the mid-span response (green dotted line) immediately jumps from zero, showing that an error occurs when the wave reaches the interface. The error of the end-node response (black dashed line) stays at zero for a little longer. It can be seen that the

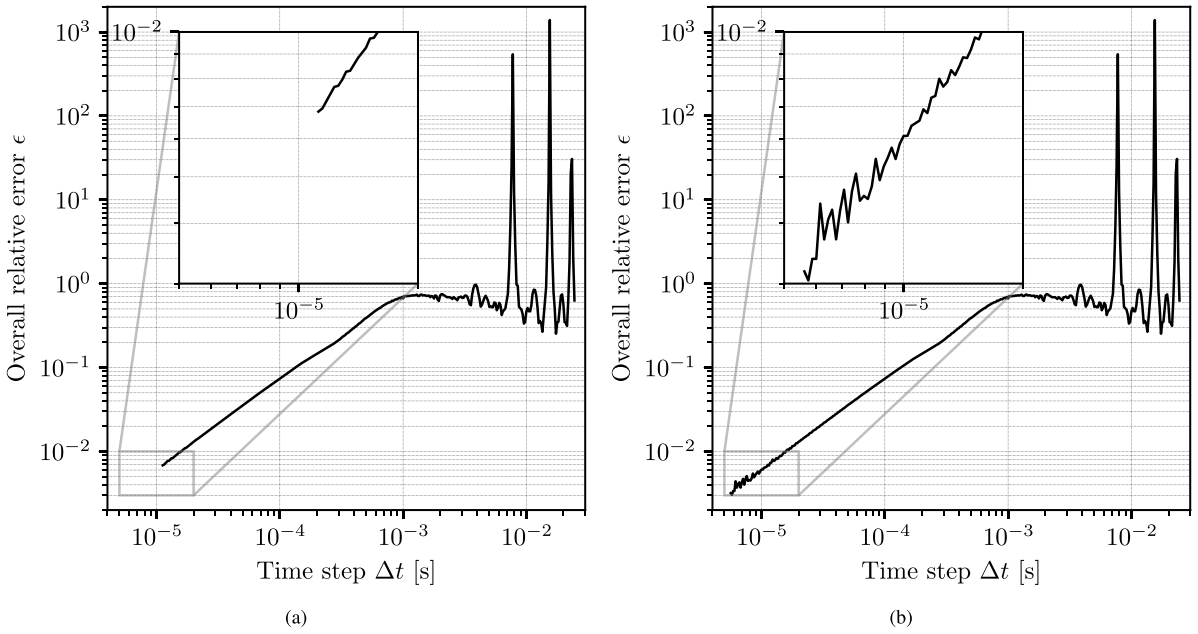

Fig. 8. BEM time step convergence: (a) one BE region and (b) two BE regions.

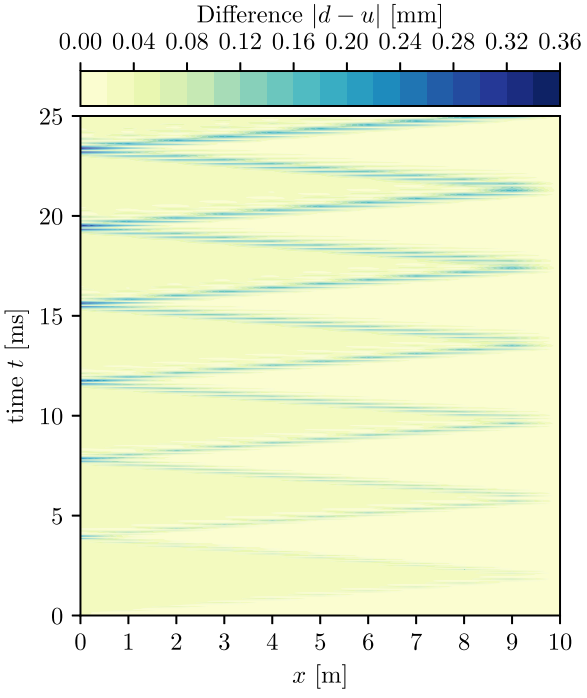

Fig. 9. Error map of pure BEM results using two regions and $\Delta t = 1 \times 10^{-5}$ s.

time to make it jump from zero is equal to twice the time to make the dotted line jump. This is due to the fact that a reflected spurious wave is originated at the interface and it takes the same time to reach the end-node as the original wave takes to reach the interface. That spurious wave will eventually reach the interface when some of it will again reflect. The original wave, in turn, will reflect at the end of the rod and reach the interface again on its way to the end-node. At that moment, part of it will once again reflect into another spurious wave. That process deteriorates the response of the coupled solution over the time of the analysis.

To highlight the presence of spurious wave reflections on the coupled solution even further, the displacement configurations at three different instants are shown in Fig. 13. These instants lie in the third oscillation cycle when the wave is travelling towards the free end-node, moving towards reestablishing the rest configuration. Fig. 13(a) shows the moment when the wave is approaching the interface. In Fig. 13(b) it can be seen that part of the incident wave reflects and travels backwards (Fig. 13(c)).

5.2. Semi-infinite homogeneous rod

The second benchmark problem is similar to the first one, with the same material and cross-section. The differences are the applied load and the fact that the domain extends towards infinity. The load is a rectangular impulse of 21 kN with 1 ms duration applied after 1 ms from the beginning of the analysis. A sketch of the example is shown in Fig. 14. DEM is employed in the first five metres of the rod, denoted as Ω_1 and BEM is used to model the remaining infinite part of the domain, referred to as Ω_2. The problem is also analysed by modelling the entire domain with BEM to have a reference solution for comparison.

The displacement of the end-node $u(0,t)$ obtained by the coupled DEM-BEM is plotted as a solid red line in Fig. 15, while the pure BEM solution is plotted as a dotted blue line. From the zoomed inset, it can be seen that the coupled DEM-BEM solution oscillates around the pure BEM solution with good agreement. The zoom inlet in Fig. 15 shows the moment when the reflected spurious wave finds the rod's end-node. That affects the end-node displacement briefly and then the spurious wave travels towards infinity again. Part of the spurious wave will again reflect on the interface giving birth to a second spurious wave. However, the amplitude of the second wave is much smaller and its effects so small that they cannot be seen in the plot.

The effect of the spurious wave reflection can be quantified by looking at the evolution of the total energy in the DEM domain. The total energy is composed of kinetic energy E_{kin} and strain energy E_{strain}. The kinetic energy E_{kin} is calculated as

$$E_{\text{kin}} = \sum_p \frac{1}{2} m_p v_p^2 \tag{30}$$

where m_p and v_p are the mass and absolute velocity of the particle p. The strain energy E_{strain} is given by

$$E_{\text{strain}} = \sum_i \frac{1}{2} k_i \delta_i^2 \tag{31}$$

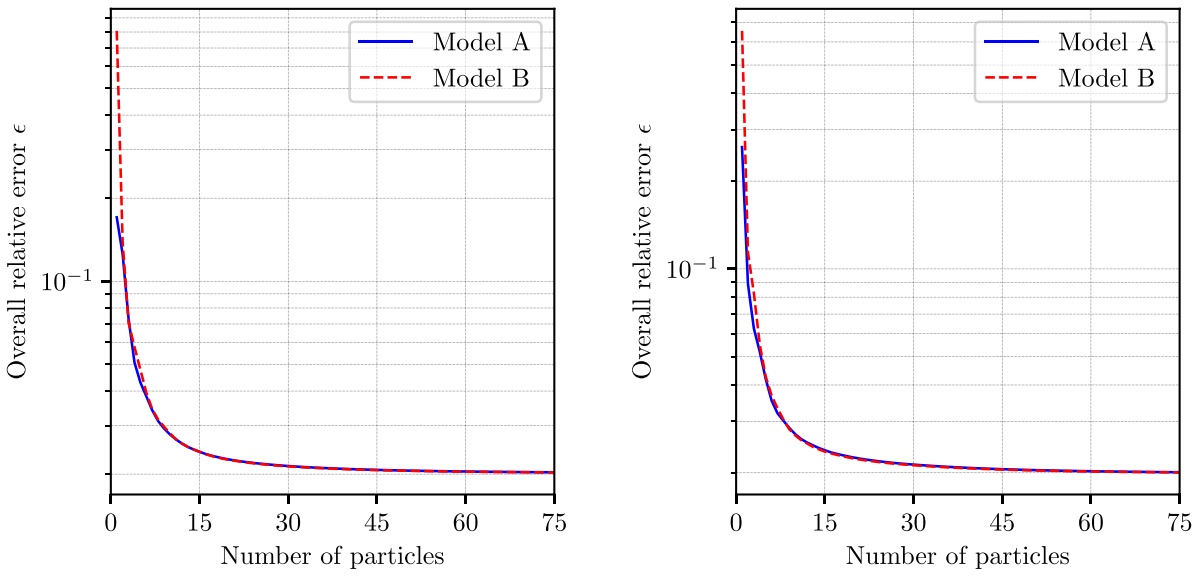

Fig. 10. DEM-BEM convergence for different interface models varying the number of DE particle with $\Delta t = 1 \times 10^{-5}$ s: (a) using DEM on the loaded part of the domain and (b) using BEM on the loaded part of the domain.

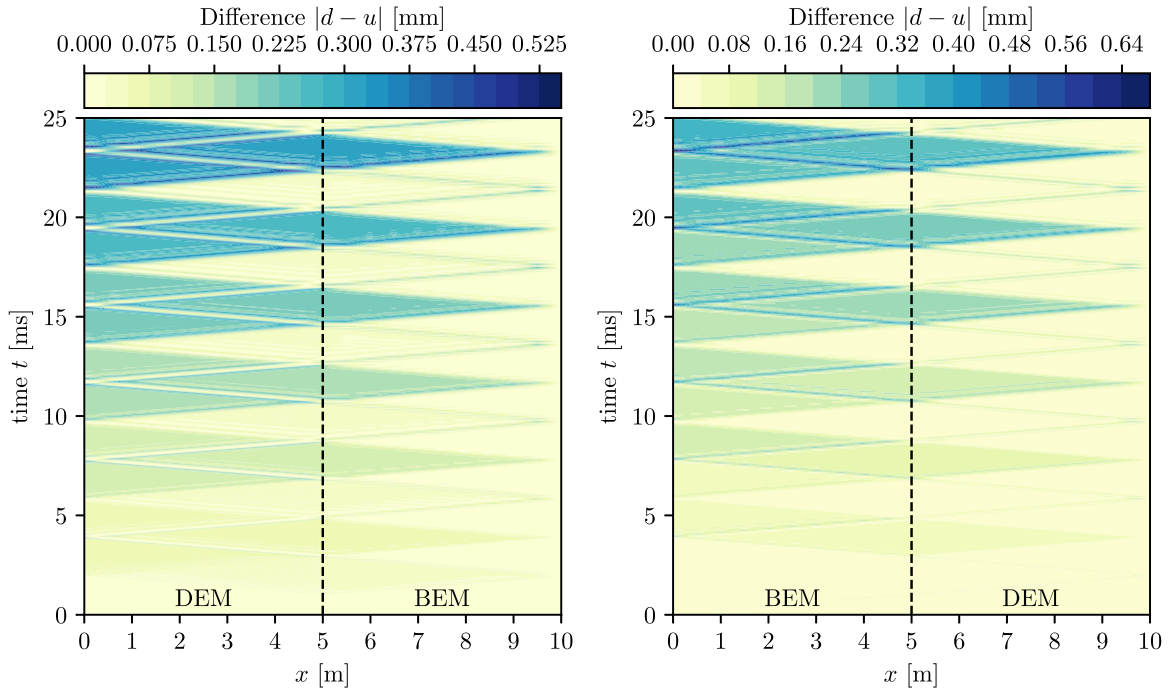

Fig. 11. DEM-BEM error maps using 50 DE particles and $\Delta t = 1 \times 10^{-5}$ s: (a) using DEM on the loaded part of the domain and (b) using BEM on the loaded part of the domain.

where k_i is the stiffness of the interaction i and δ_i is the relative displacement of the two particles of interaction i. Hence, if particles p and q are interacting through interaction i, $k_i = k_{pq}$, as defined in Eq. (10), and $\delta_i = |d_p - d_q|$.

Fig. 16 shows the evolution of the energy in the DEM domain. The total energy of the DEM domain is shown by a solid blue line, while its components, the kinetic and strain energy are shown in dashed red and dotted green lines, respectively. The total energy theoretically has to drop to zero as the wave travels from the DEM into the BEM domain at around 4 ms. Nevertheless, it can be seen that a small amount of energy of about 1.2 J is still in the DEM domain at 4 ms. This residual energy results from the spurious wave reflection. The amount is less than 0.7 % of the total 178 J energy of the system. This confirms that the effect of spurious wave reflection is indeed negligible. It can also be seen that this effect decreases over time, *i.e.* the energy asymptotically tends to zero as the wave travels to infinity in the BEM domain.

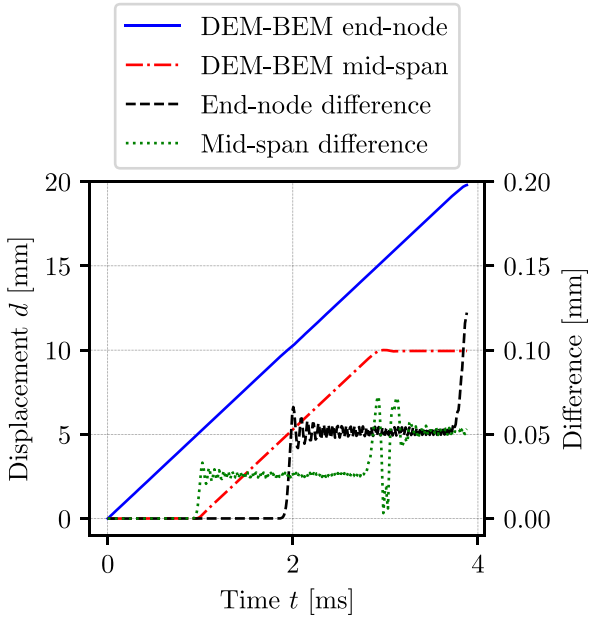

Fig. 12. Difference between coupled DEM-BEM and pure DEM solutions. The coupled DEM-BEM approach uses 76 particles with interface Model A. The pure DEM model uses 151 particles. In both analyses the time step is $\Delta t = 1 \times 10^{-5}$ s. (For interpretation of the references to colour in this figure legend, the reader is referred to the web version of this article.)

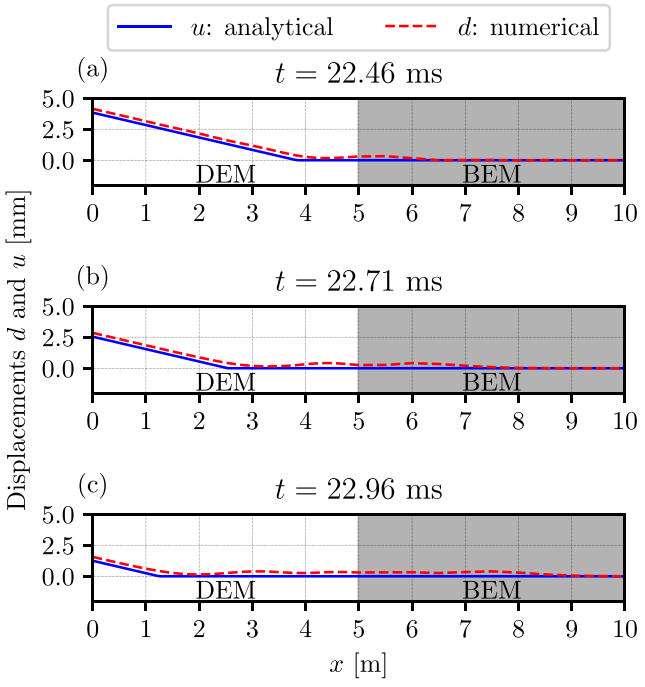

Fig. 13. Displacement configuration calculated using 75 DE particles and $\Delta t = 1 \times 10^{-5}$ s at: (a) $t = 22.46$ ms, (b) $t = 22.71$ ms and (c) $t = 22.96$ ms. See Appendix online version for video.

5.3. Semi-infinite non-homogeneous rod

The third benchmark problem is a non-homogeneous rod composed of two different materials as also discussed in Moser et al. [35]. One of the materials extends to infinity, as shown in Fig. 17. The problem is modelled with the coupled DEM-BEM approach modelling Ω_1 (finite domain) with DEM and Ω_2 (infinite domain) with BEM. The problem is also modelled with BEM on both domains for comparison.

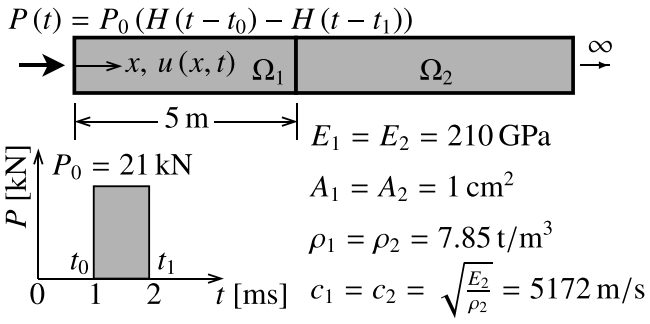

Fig. 14. Semi-infinite homogeneous rod loaded with a rectangular impulse.

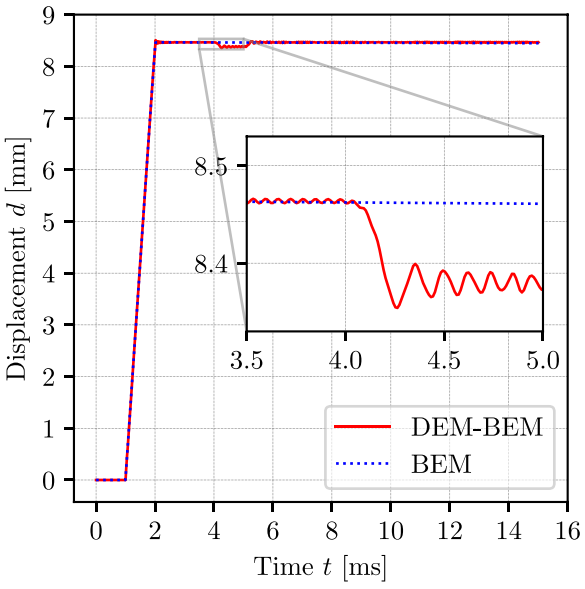

Fig. 15. End-node displacement of semi-infinite homogeneous rod: comparison between coupled DEM-BEM and pure BEM solution, using 76 particles in the DEM domain and $\Delta t = 1 \times 10^{-2}$ ms in both analyses. (For interpretation of the references to colour in this figure legend, the reader is referred to the web version of this article.)

The responses of the end-node displacement using the coupled DEM-BEM and the pure BEM approaches are plotted in Fig. 18. The displacement initially tends to the solution as though the rod was made only of the first material since all the deformation is in the first rod. When the wave reaches the interface, a normal reflection occurs which makes the end-node displacement drop. The reflected wave reflects at the end-node and travels back to the interface where part of it passes on to the other domain and another part reflects. That cyclic behaviour keeps going until the reflection tends to zero, at which point the displacement is as though the rod was entirely made of the second material, as the majority of deformation, waves are within this media travelling towards infinity.

On top of that behaviour, which is expected, there is the spurious wave reflection phenomenon, which is evidenced in Fig. 18. Compared with the pure BEM approach, the DEM-BEM coupled solution introduces more noise. In other words, the coupled solution oscillates around the pure BEM solution. But yet, that influence can be neglected as the dynamic response of the system is captured very well.

6. Conclusions

In this paper, an interface DEM-BEM coupling approach in the time domain for multi-scale modelling is presented. The modifications

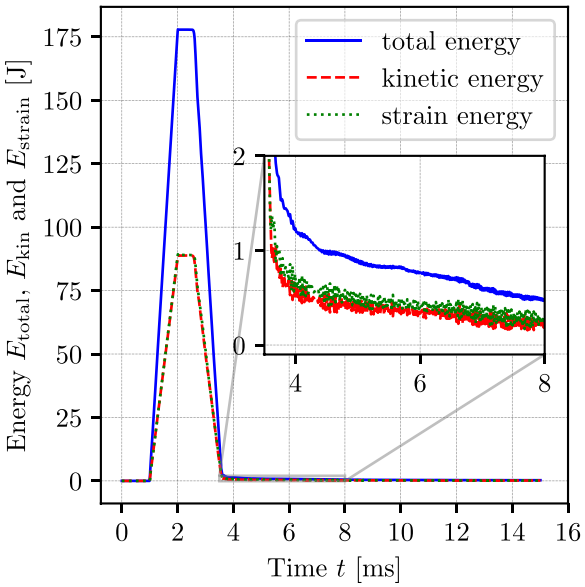

Fig. 16. Energy evolution in the DEM domain, using 76 particles in the DEM domain and $\Delta t = 1 \times 10^{-2}$ ms. (For interpretation of the references to colour in this figure legend, the reader is referred to the web version of this article.)

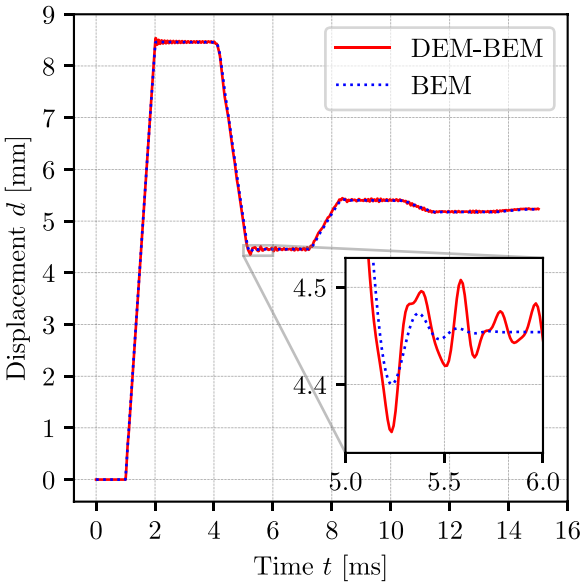

Fig. 18. End-node displacement of semi-infinite non-homogeneous rod: comparison between coupled DEM-BEM using 76 particles and pure BEM solution, both using $\Delta t = 1 \times 10^{-2}$ ms.

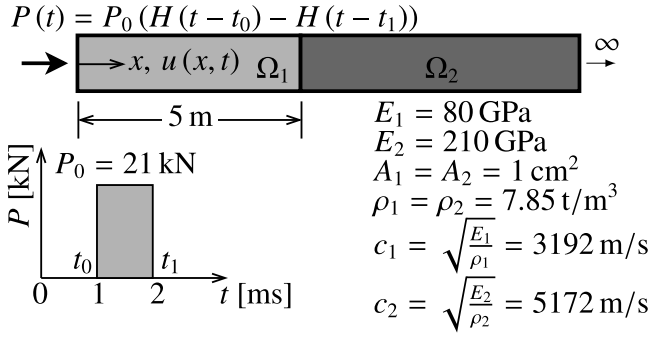

Fig. 17. Semi-infinite non-homogeneous rod loaded with a rectangular impulse.

required in both methods to make the coupling possible are discussed. The CD time integration scheme is proposed for the DEM instead of the most commonly used "leapfrog". This allows for the formulation of a dynamic stiffness equilibrium equation. On the BEM side, the dynamic stiffness equilibrium equation is written as a convolution integral, which is solved employing the CQM.

The proposed interface coupling approach has proven itself to be of simple formulation. The phenomenon of spurious wave reflection also reported by other authors for DEM-FEM coupling [14,22] was also observed in the current DEM-BEM coupling. In the finite rod example, the spurious wave is confined, and as the analysis goes on more spurious waves are generated. Nevertheless, it is shown that the effect of spurious wave reflection is negligible for semi-infinite domain problems. The wave travels towards infinity and does not disturb the solution cumulatively over time. A quantitative analysis of the effect shows that the energy reflected at the interface is less than 0.7 % of the total energy and it tends to decay quickly over time. Hence, the presented approach is very suitable for handling applications with semi-infinite and infinite domains which is the main motivation for coupling DEM with BEM.

Another key finding of this work is related to the time step. The time step in the explicit DEM formulation has an upper bound, the critical time step, so that the numerical analysis is stable. This time step depends not only on the parameters of the problem but also on the spatial discretisation used. The finer the discretisation the smaller the critical time step. The BEM has a range of time steps within which the simulations are stable. This paper shows that subdividing the problem's domain into multiple BEM regions, using the same time step, does not change the method's accuracy. However, the multi-region approach allows decreasing the lower bound of the time step. Thus, higher accuracy can be achieved by lowering the time step. An inquiry that hung over this research before it started was whether there would be an intersection between the time step required for the stability of the two methods. This intersection is vital for the coupled solution to be numerically stable. This paper shows that such intersection indeed exists. Additionally, it can be concluded that whenever the DEM requires a time step lower than what can be used in the BEM, the multi-region BEM approach can be used to make the coupling feasible.

Although this paper is focused on one-dimensional analyses, its findings led to important knowledge as to what can be expected for analyses in two- and three-dimensions. The latter will be considered in future research with focus on geomechanics problems where the infinite and discontinuous nature of the ground is of paramount importance.

CRediT authorship contribution statement

Guilherme Barros: Methodology, Software, Formal analysis, Investigation, Data curation, Writing – original draft, Writing – review & editing, Visualisation. **Andre Pereira:** Conceptualization, Methodology, Writing – review & editing, Supervision. **Jerzy Rojek:** Conceptualization, Methodology, Writing – review & editing, Supervision, Funding acquisition. **Klaus Thoeni:** Conceptualization, Methodology, Writing – review & editing, Visualization, Supervision, Project administration, Funding acquisition.

Acknowledgement

The authors would like to acknowledge the financial support of the Australian Research Council (DP1901024707).

Appendix A. Supplementary data

Supplementary material related to this article can be found online at https://doi.org/10.1016/j.enganabound.2021.10.017.

References

[1] Achenbach J. Wave propagation in elastic solids. Elsevier; 2012.

[2] Rojek J, Madan N, Nosewicz S. Micro–macro relationships in the simulation of wave propagation phenomenon using the discrete element method. Materials 2019;12(24):4241. http://dx.doi.org/10.3390/ma12244241.

[3] Cundall PA, Strack ODL. A discrete numerical model for granular assemblies. Géotechnique 1979;29(1):47–65. http://dx.doi.org/10.1680/geot.1979.29.1.47.

[4] Cundall PA. A discontinuous future for numerical modelling in geomechanics? Proc Inst Civil Eng - Geotech Eng 2001;149(1):41–7. http://dx.doi.org/10.1680/geng.2001.149.1.41.

[5] Rousseau J, Frangin E, Marin P, Daudeville L. Multidomain finite and discrete elements method for impact analysis of a concrete structure. Eng Struct 2009;31(11):2735–43. http://dx.doi.org/10.1016/j.engstruct.2009.07.001.

[6] Li M, Yu H, Wang J, Xia X, Chen J. A multiscale coupling approach between discrete element method and finite difference method for dynamic analysis. Internat J Numer Methods Engrg 2015;102(1):1–21. http://dx.doi.org/10.1002/nme.4771.

[7] Campbell CS. Rapid granular flows. Annu Rev Fluid Mech 1990;22(1):57–90. http://dx.doi.org/10.1146/annurev.fl.22.010190.000421.

[8] Williams JR, O'Connor R. Discrete element simulation and the contact problem. Arch Comput Methods Eng 1999;6(4):279–304. http://dx.doi.org/10.1007/BF02818917.

[9] Cook BK, Jensen RP. Discrete element methods. numerical modeling of discontinua. American Society of Civil Engineers; 2002, http://dx.doi.org/10.1061/9780784406472.

[10] Rojek J, Oñate E, Labra C, Kargl H. Discrete element simulation of rock cutting. Int J Rock Mech Min Sci 2011;48(6):996–1010. http://dx.doi.org/10.1016/J.IJRMMS.2011.06.003.

[11] Konietzky H. Numerical Modeling in Micromechanics Via Particle Methods. London: Routledge; 2017, p. 334. http://dx.doi.org/10.1201/9780203745335.

[12] Oñate E, Rojek J. Combination of discrete element and finite element methods for dynamic analysis of geomechanics problems. Comput Methods Appl Mech Engrg 2004;193(27–29):3087–128. http://dx.doi.org/10.1016/j.cma.2003.12.056.

[13] Azevedo NM, Lemos JV. Hybrid discrete element/finite element method for fracture analysis. Comput Methods Appl Mech Engrg 2006;195(33–36):4579–93. http://dx.doi.org/10.1016/j.cma.2005.10.005.

[14] Rojek J, Oñate E. Multiscale analysis using a coupled discrete/finite element model. Interact Multiscale Mech 2008;1(1):1–31. http://dx.doi.org/10.12989/imm.2008.1.1.001.

[15] Xiao SP, Belytschko T. A bridging domain method for coupling continua with molecular dynamics. Comput Methods Appl Mech Engrg 2004;193(17–20):1645–69. http://dx.doi.org/10.1016/j.cma.2003.12.053.

[16] Elmekati A, Shamy UE. A practical co-simulation approach for multiscale analysis of geotechnical systems. Comput Geotech 2010;37(4):494–503. http://dx.doi.org/10.1016/j.compgeo.2010.02.002.

[17] Li X, Wan K. A bridging scale method for granular materials with discrete particle assembly - cosserat continuum modeling. Comput Geotech 2011;38(8):1052–68. http://dx.doi.org/10.1016/j.compgeo.2011.07.001.

[18] Wellmann C, Wriggers P. A two-scale model of granular materials. Comput Methods Appl Mech Engrg 2012;205–208(1):46–58. http://dx.doi.org/10.1016/j.cma.2010.12.023.

[19] Dang HK, Meguid MA. An efficient finite-discrete element method for quasi-static nonlinear soil-structure interaction problems. Int J Numer Anal Methods Geomech 2013;37(2):130–49. http://dx.doi.org/10.1002/nag.1089.

[20] Xu W, Zang M. Four-point combined DE/FE algorithm for brittle fracture analysis of laminated glass. Int J Solids Struct 2014;51(10):1890–900. http://dx.doi.org/10.1016/j.ijsolstr.2014.01.026.

[21] Tu F, Ling D, Bu L, Yang Q. Generalized bridging domain method for coupling finite elements with discrete elements. Comput Methods Appl Mech Engrg 2014;276:509–33. http://dx.doi.org/10.1016/j.cma.2014.03.023.

[22] Tu F, Ling D, Hu C, Zhang R. DEM-FEM analysis of soil failure process via the separate edge coupling method. Int J Numer Anal Methods Geomech 2017;41(9):1157–81. http://dx.doi.org/10.1002/nag.2666.

[23] Tu F, Jiao Y, Chen Z, Zou J, Zhao Z. Stress continuity in DEM-fem multiscale coupling based on the generalized bridging domain method. Appl Math Model 2020;83:220–36. http://dx.doi.org/10.1016/j.apm.2020.02.030.

[24] Miller RE, Tadmor EB. A unified framework and performance benchmark of fourteen multiscale atomistic/continuum coupling methods. Modelling Simulation Mater Sci Eng 2009;17(5):053001. http://dx.doi.org/10.1088/0965-0393/17/5/053001.

[25] Wagner GJ, Liu WK. Coupling of atomistic and continuum simulations using a bridging scale decomposition. J Comput Phys 2003;190(1):249–74. http://dx.doi.org/10.1016/S0021-9991(03)00273-0.

[26] Aubertin P, Réthoré J, de Borst R. Energy conservation of atomistic/continuum coupling. Internat J Numer Methods Engrg 2009;78(11):1365–86. http://dx.doi.org/10.1002/nme.2542.

[27] Aubertin P, Réthoré J, de Borst R. A coupled molecular dynamics and extended finite element method for dynamic crack propagation. Internat J Numer Methods Engrg 2009;81(1):72–88. http://dx.doi.org/10.1002/nme.2675.

[28] Beer G, Watson JO. Infinite boundary elements. Internat J Numer Methods Engrg 1989;28(6):1233–47. http://dx.doi.org/10.1002/NME.1620280602.

[29] Brebbia CA. The boundary element method for engineers. London: Pretech Press; 1978.

[30] Dominguez J. Boundary elements in dynamics. London: Elsevier Applied Science; 1993, p. 450.

[31] Schanz M. Wave propagation in viscoelastic and poroelastic continua: a boundary element approach. Berlin: Springer-Verlag; 2001, http://dx.doi.org/10.1007/978-3-540-44575-3.

[32] Lorig LJ, Brady BHG, Cundall PA. Hybrid distinct element-boundary element analysis of jointed rock. Int J Rock Mech Min Sci Geomech Abstr 1986;23(4):303–12. http://dx.doi.org/10.1016/0148-9062(86)90642-X.

[33] Huang A-B, Ma MY, Lee JS. A micromechanical study of penetration tests in granular material. Mech Mater 1993;16(1–2):133–9. http://dx.doi.org/10.1016/0167-6636(93)90036-Q.

[34] Malinowski L, Karlis GF, Beer G, Rojek J. Iterative coupling of boundary and discrete element methods using an overlapping fem zone. In: COUPLED IV: Proceedings of the IV international conference on computational methods for coupled problems in science and engineering. CIMNE; 2011, p. 301–12.

[35] Moser W, Antes H, Beer G. A Duhamel integral based approach to one-dimensional wave propagation analysis in layered media. Comput Mech 2005;35(2):115–26. http://dx.doi.org/10.1007/s00466-004-0607-8.

[36] Pereira AMB, Beer G. Interface dynamic stiffness matrix approach for three-dimensional transient multi-region boundary element analysis. Internat J Numer Methods Engrg 2009;80(11):1463–95. http://dx.doi.org/10.1002/nme.2680.

[37] Otsubo M, O'Sullivan C, Shire T. Empirical assessment of the critical time increment in explicit particulate discrete element method simulations. Comput Geotech 2017;86:67–79. http://dx.doi.org/10.1016/j.compgeo.2016.12.022.

[38] Clough RW, Penzien J. Dynamics of structures. McGraw-Hill Book Company; 1975.

[39] Timoshenko SP, Young DH, Weaver W. Vibration problems in engineering. New York, NY: Wiley; 1974.

[40] Mansur WJa, Brebbia CA. Formulation of the boundary element method for transient problems governed by the scalar wave equation. Appl Math Model 1982;6(4):307–11. http://dx.doi.org/10.1016/S0307-904X(82)80039-5.

[41] Lubich C. Convolution quadrature and discretized operational calculus. I. Numer Math 1988;52(2):129–45. http://dx.doi.org/10.1007/BF01398686.

[42] Lubich C. Convolution quadrature and discretized operational calculus. II. Numer Math 1988;52(4):413–25. http://dx.doi.org/10.1007/BF01462237.

[43] Chopra A. Dynamics of structures, vol. 1. fourth ed.. Prentice Hall; 2011, p. 980. http://dx.doi.org/10.1016/0045-7825(92)90174-I.